Fluid-wall interactions in pseudopotential lattice Boltzmann models

Cheng Peng [*]

*Key Laboratory of High Efficiency and Clean Mechanical Manufacture, Ministry of Education,
School of Mechanical Engineering, Shandong University, Jinan 250061, China
and Department of Energy and Mineral Engineering and EMS Energy Institute,
The Pennsylvania State University, University Park, Pennsylvania 16802, USA*

Luis F. Ayala

*Department of Energy and Mineral Engineering, EMS Energy Institute,
The Pennsylvania State University, University Park, Pennsylvania 16802, USA*

Orlando M. Ayala

Department of Engineering Technology, 111A Kaufman Hall, Old Dominion University, Norfolk, Virginia 23529, USA

Designing proper fluid-wall interaction forces to achieve proper wetting conditions is an important area of interest in pseudopotential lattice Boltzmann models. In this paper, we propose a modified fluid-wall interaction force that applies for pseudopotential models of both single-component fluids and partially miscible multicomponent fluids, such as hydrocarbon mixtures. A reliable correlation that predicts the resulting liquid contact angle on a flat solid surface is also proposed. This correlation works well over a wide variety of pseudopotential lattice Boltzmann models and thermodynamic conditions.

I. INTRODUCTION

Pseudopotential (PP) lattice Boltzmann (LB) models are among one of the most popular categories of LB models for a variety of multiphase flow simulation scenarios [1]. Their popularity comes mainly from their simplicity in concept and easiness to implement [2,3]. The idea of PP LB models is to introduce a fully discretized external body force to the Navier-Stokes (N-S) equations to facilitate multiphase flow simulations. This force serves two purposes: it not only provides a mechanism to separate phases, but also introduces a surface tension force due to interfacial curvature that balances the (capillary) pressure difference between the phases [4,5].

There are two categories of PP LB models, single-component (SC) PP LB models and multicomponent (MC) PP LB models. In the former, the designed external body force modifies the linear relationship between the pressure and the fluid density reproduced by the standard LB models, so fluids are driven towards two equilibrium states with distinct densities [2,3]. MC PP LB models, on the other hand, have been largely restricted to applications when components are fully immiscible, i.e., each component forms its own phase and does not significantly dissolve in the other phases [6,7]. In this category, external body forces are designed as repulsive forces for individual components to prevent them from mixing. Only until recently, MC PP LB models for partially miscible multicomponent fluids (PMMCFs) were proposed

[8,9]. PMMCFs are referred to fluids, such as hydrocarbon mixtures where components are present in all phases but at different concentrations, whereas phases remain partially miscible with each other [10,11]. Using gasoline as an example, when it forms a vapor-liquid (vl) two-phase system, all the hydrocarbon components would exist in both phases, but their molar fractions in the two phases are usually vastly different due to their different volatility. Within each phase, i.e., vapor or liquid, all hydrocarbon components form a homogeneous mixture. To accommodate a system of PMMCFs, the external body force of a PP LB model must be defined in terms of phases to bring in thermodynamic information that correctly distribute components into phases [8,9]. Then this force is split to individual components based on their volatility to evolve the distribution functions in the LB model [9].

In many applications, such as porous media flow, the ability to handle wetting conditions on solid surfaces is a crucial step towards achieving realistic multiphase flow simulations. In PP LB models, the wetting conditions can be easily achieved with properly designed fluid-wall interaction forces [7,12–16]. The definitions of such fluid-wall interaction forces are similar to those fluid-fluid external body force. In those MC PP LB models applied to fully immiscible components, specific wetting conditions are realized by making the wall adhesive to wetting fluids and repulsive to nonwetting fluids. This is controlled by the signs of adhesive parameters of the designed fluid-wall interaction forces applied to individual components [7]. Later, Huang *et al.* discovered that the wetting condition actually depended on the difference between the adhesive parameters

---
*czp341@psu.edu

rather than their individual values [14]. Another contribution of Huang *et al.* was to build an empirical formula to anticipate contact angles with respect to adhesive parameter differences in immiscible MC PP LB models.

The above scheme for MC PP LB models had been modified to function in SC PP LB models where the intensity of the fluid-wall interaction force controls the resulting liquid contact angles [12,13]. Another popular way to handle wetting conditions in SC PP LB models is the virtual density method proposed by Benzi *et al.* [17]. This scheme sets a constant virtual fluid density at solid nodes, then uses this virtual density to define the pseudopotential and the fluid-wall interaction force sequentially. By adjusting the virtual density from the liquid density to vapor density, one can change the liquid contact angle from 0°e to 180° [17]. A main issue of the above schemes is that they can cause a nonphysical mass transfer layer between the droplet and the solid surface as reported by Li *et al.* [16]. These schemes could also cause relatively large spurious currents near fluid-wall interfaces. Recently, Li *et al.* proposed an improved scheme for fluid-wall interaction forces [16]. Instead of using a constant virtual density to define the pseudopotential at the wall, Li *et al.* adopted the weighted local averaged density. This simple improvement was shown to effectively eliminate the nonphysical mass transfer layer and suppress spurious currents.

Although these aforementioned fluid-wall interaction schemes are able to achieve different wetting conditions in SC PP LB models via adjusting their tuning parameters, further improvements remain to be performed in two aspects. First, functional dependencies or empirical correlations, such as the one built by Huang *et al.* [14] for MC PP LB of fully immiscible fluids, remain still absent for the purpose of linking tuning parameters to contact angles. From the users' point of view, a trial and error process is required to find the values of those tuning parameters for any desired wetting condition, given that the values of those parameters are largely case dependent. Second, there is no scheme to realize the wetting conditions in MC PP LB models for PMMCFs, which largely constrains the applications of our proposed model. As we will discuss later, the available fluid-wall interaction schemes that work well for pure component cases would have some difficulties to be straightforwardly extend to PMMCF scenarios.

The present paper aims at solving the above two deficiencies. First, enlightened by the study of Li *et al.* [16], we will design a further simplified fluid-wall interaction scheme that achieves wetting conditions for both SC fluids and PMMCFs. Second, based on the modified scheme, we will summarize an empirical correlation to predict the resulting contact angles. This correlation is applicable for both SC and PMMCF cases and covers a wide variety of thermodynamic conditions. Compared to its alternatives, the modified scheme mainly has the advantages on the easiness to implement, and the capability to function with MC PP LB models for PMMCFs.

The remaining paper is arranged as follows. In Sec. II, we will give a brief introduction on SC PP LB models and MC PP LB models for PMMCFs and review some representative fluid-wall interaction schemes. Then, in Sec. III, we will propose the simplified fluid-wall interaction scheme and formulate the empirical correlation to predict the resulting contact angles. Validations of the proposed scheme and

empirical correlation will be conducted in Sec. IV. Finally, the main conclusions of the paper will be recapitulated in Sec. V.

II. PSEUDOPOTENTIAL LATTICE BOLTZMANN MODELS AND FLUID-WALL INTERACTION

A. Pseudopotential lattice Boltzmann models

The standard lattice Boltzmann method can be viewed as an indirect solver of the N-S equations [18]. It tracks the evolution of distribution functions for a selected set of discrete velocities. The evolution equation of the distribution function is known as the lattice Boltzmann equation (LBE). With the multirelaxation time (MRT) collision operator, LBE can be written as

$$
\begin{aligned}
f_\alpha(\mathbf{x} &+ \mathbf{e}_\alpha \delta_t, t + \delta_t) - f_\alpha(\mathbf{x}, t) \\
&= -(\mathbf{M}^{-1}\mathbf{S})_{\alpha\beta}\big[m_\beta(\mathbf{x}, t) - m_\beta^{(eq)}(\mathbf{x}, t)\big] \\
&\quad + \left[\mathbf{M}^{-1}\left(\mathbf{I} - \frac{\mathbf{S}}{2}\right)\right]_{\alpha\beta} \Theta_\beta(\mathbf{x}, t)\delta t,
\end{aligned}
\tag{1}
$$

where f_α is the distribution function corresponding to the αth discrete velocity $\mathbf{e}_\alpha$ among the selected discrete velocities, $\mathbf{x}$ and t represent the current spatial location and time, respectively, δ_t is the time step size, $\mathbf{M}^{-1}$ is the inverse of the transform matrix $\mathbf{M}$, which converts the distribution functions into the same amount of moments, $\mathbf{S}$ is the diagonal matrix of relaxation frequencies (i.e., the reciprocals of the relaxation times). For a D2Q9 discrete velocity set, $\mathbf{S} = \text{diag}[\tau_\rho^{-1}, \tau_e^{-1}, \tau_\varepsilon^{-1}, \tau_j^{-1}, \tau_q^{-1}, \tau_j^{-1}, \tau_q^{-1}, \tau_\nu^{-1}, \tau_\nu^{-1}]$, where τ_ρ, τ_e, τ_ε, τ_j, τ_q, and τ_ν are relaxation times of the density, energy, energy square, momentum, energy flux, and viscous stress moment, respectively [19]. m_β is the βth moment, and $m_\beta^{(eq)}$ stands for its equilibrium part. Finally, Θ_β is the moment form of forcing term for the βth moment.

The above LB model reproduces the continuity and momentum equations in the N-S equation system. The hydrodynamic quantities, such as fluid density ρ, and velocity $\mathbf{u}$ are related to the distribution functions as [20]

$$
\rho = \sum_\alpha f_\alpha, \quad \rho\mathbf{u} = \sum_\alpha \mathbf{e}_\alpha f_\alpha + \frac{\delta_t}{2}\mathbf{F},
\tag{2}
$$

where $\mathbf{F}$ is the body force in N-S equations.

PP LB models realize multiphase flow simulations by introducing a fluid-fluid interaction force that mimics that of the molecular interactions. For SC fluids, this force is often defined as [2]

$$
\mathbf{F}(\mathbf{x}) = -G\psi(\mathbf{x})\sum_\alpha w_\alpha \psi(\mathbf{x} + \mathbf{e}_\alpha \delta_t)\mathbf{e}_\alpha,
\tag{3}
$$

where G is the intensity of the interaction force, $\psi(\mathbf{x})$ is the pseudopotential at the current location, and $\psi(\mathbf{x} + e_\alpha \delta_t)$ are the pseudopotentials on its neighboring locations with w_α being the weights. To incorporate thermodynamic information of real fluids into the model to guide phase transition, the pseudopotential ψ is usually defined via the cubic equations of state (EOS) [21],

$$
\psi = \sqrt{\frac{2[p_{EOS}(\rho) - c_s^2\rho]}{Gc_s^2\delta_t}},
\tag{4}
$$

where p_{EOS} is the pressure predicted by the selected cubic EOS, c_s is the speed of sound, which is a constant associated to the selected discrete velocity set. It should be noted that when the pseudopotential is defined in this way, G no longer controls the intensity of the fluid-fluid interaction force but only needs to ensure the non-negativity of whole term under the square root [21].

A well-recognized issue of the above SC PP LB model is its thermodynamic inconsistency, which means, the resulting two-phase densities in a simulation, especially the vapor phase density, would significantly deviate from the values predicted by the selected cubic EOS [22–24]. This is because as ψ has been determined by Eq. (4), there is no extra degree of freedom to satisfy the chemical balance condition simultaneously, i.e., the two phases having the same chemical potential [24]. There are several remedies to introduce additional degrees of freedom to restore thermodynamic consistency [22,24–26]. A frequently used remedy is the modified forcing scheme proposed by Li *et al.* [26]. In this scheme, the two forcing terms associated with the energy and energy square moments are defined as

$$
\begin{aligned}
\Theta_e &= 6\mathbf{F} \cdot \left(\mathbf{u} + \frac{\sigma \mathbf{F}}{(\tau_e - 0.5)c_s^2 \delta_t \psi^2} \right), \\
\Theta_\epsilon &= -6\mathbf{F} \cdot \left(\mathbf{u} + \frac{\sigma \mathbf{F}}{(\tau_\varepsilon - 0.5)c_s^2 \delta_t \psi^2} \right),
\end{aligned}
\tag{5}
$$

where σ is a free parameter whose value is tuned to restore thermodynamic consistency. u, v, and F_x, F_y are the components of the fluid velocity and force, respectively. The other forcing terms are kept the same as those in the standard MRT collision operator, which is not repeated here. In the present paper, the forcing scheme of Li *et al* would be used as the default scheme in numerical tests, unless otherwise specified.

In MC PP LB models, each component is assigned with a separated set of distribution functions, whose evolution is tracked by the same LBE in Eq. (1). However, unlike SC PP LB models, the fluid density and velocity in MC PP LB models are computed as

$$
\bar{\rho}_\eta = \sum_\alpha f_{\alpha,\eta}, \quad \rho = \sum_\eta \bar{\rho}_\eta,
$$

$$
\rho \mathbf{u} = \sum_\eta \left(\sum_\alpha \mathbf{e}_\alpha f_{\alpha,\eta} + \frac{\delta_t}{2} \mathbf{F}_\eta \right),
\tag{6}
$$

where quantities with a subscript η are associated with the individual component η in the system. Different from fully immiscible fluids where no mass transfer happens at the two-fluid interface, phases of partially miscible fluids can exchange masses to establish new thermodynamic equilibrium states, in response to the changes in temperature, pressure, and phase compositions. In these processes, thermodynamic information plays a crucial role in guiding how components are redistributed among phases [27,28]. It should be noted that $\bar{\rho}$ with an overbar in Eq. (6) refers to the "densities of components," which has no thermodynamic significance for PMMCFs [9].

The same as SC PP LB models, the thermodynamic information is introduced to MC PP LB models via using

cubic EOS, e.g., the Peng-Robinson EOS [29], to define the pseudopotential. For the sake of conciseness, the procedure is briefly summarized as follows: (1) The local molar density $\tilde{\rho}$ and the local molar fraction are input into the cubic EOS for PMMCFs to compute the thermodynamic pressure p_{EOS}. (2) Together with the mass density of the phase ρ, the pseudopotential ψ and the total fluid-fluid interaction force applied to the phase are defined via Eqs. (4) and (3), respectively. (3) This total interaction force is then split to individual components so the distribution functions can evolve [8,9]. More details on the MC PP LB model for PMMCFs can be found in Ref. [9], which are no longer repeated here.

B. Fluid-wall interaction

As mentioned before, wetting conditions in the PP LB models are achieved via fluid-wall interaction forces. One of the most commonly used fluid-wall interaction schemes is formulated by Sukop and Thorne [13] as

$$
\mathbf{F}_w(\mathbf{x}) = -G_w \psi(\mathbf{x}) \sum_\alpha w_\alpha s(\mathbf{x} + \mathbf{e}_\alpha \delta_t) \mathbf{e}_\alpha,
\tag{7}
$$

where G_w is the intensity of the fluid-wall interaction, $s(\mathbf{x} + \mathbf{e}_\alpha \delta_t)$ is a solid phase indicator which equals 1 if the location $(\mathbf{x} + \mathbf{e}_\alpha \delta_t)$ is a solid node and 0 otherwise. With this scheme, the liquid contact angle is adjusted via tuning G_w. In general, the negative values of G_w often result in hydrophilic wetting conditions, i.e., a liquid contact angle $\theta < 90°$, whereas positive values of G_w lead to hydrophobic wetting conditions, i.e., $\theta > 90°$. The small G_w is the smaller the contact angle θ would be.

Another popular scheme of fluid-wall interaction in SC PP LB models was proposed by Benzi *et al.* [17], which relies on a constant virtual density ρ_w to achieve wetting conditions. This fluid-wall interaction scheme can be expressed as

$$
\mathbf{F}_w(\mathbf{x}) = -G \psi(\mathbf{x}) \sum_\alpha w_\alpha \psi(\rho_w) s(\mathbf{x} + \mathbf{e}_\alpha \delta_t) \mathbf{e}_\alpha,
\tag{8}
$$

where $\psi(\rho_w)$ is the constant pseudopotential at solid nodes defined by Eq. (4). Although in the work of Benzi *et al.* [17] an analytic correlation was provided to determine ρ_w for the desired contact angle θ, in practice, tuning ρ_w through trial and error is still inevitable.

The above two schemes can generate a undesired nonphysical mass transfer layer between a staying droplet and the solid wall [16]. To eliminate this nonphysical mass transfer layer, Li *et al.* proposed using the local fluid density rather than the constant virtual density to define the fluid-wall interaction force, i.e., the constant virtual density ρ_w in the scheme of Benzi *et al.* was modified as [16]

$$
\rho_w(\mathbf{x}) = \begin{cases} \phi \rho_{ave}(\mathbf{x}), & \phi > 1 \quad \text{for} \quad \theta < 90°, \\ \rho_{ave}(\mathbf{x}) - \Delta\rho, & \Delta\rho > 0 \quad \text{for} \quad \theta > 90°, \end{cases}
\tag{9}
$$

where

$$
\rho_{ave}(\mathbf{x}) = \frac{\sum_\alpha w_\alpha s'(\mathbf{x} + \mathbf{e}_\alpha \delta_t) \rho(\mathbf{x} + \mathbf{e}_\alpha \delta_t)}{\sum_\alpha w_\alpha s'(\mathbf{x} + \mathbf{e}_\alpha \delta_t)}.
\tag{10}
$$

Here $s'(\mathbf{x} + \mathbf{e}_\alpha \delta_t)$ is a fluid phase indicator which equals 1 if $(\mathbf{x} + \mathbf{e}_\alpha \delta_t)$ is a fluid node and 0 otherwise. It should be noted that a limiter is applied to confine $\rho_w(\mathbf{x})$ between the saturated

vapor density $\rho_{v,\text{sat}}$ and the saturated liquid density $\rho_{l,\text{sat}}$ at a given temperature. The two tuning parameters ϕ and $\Delta\rho$ are adjusted to achieve the desired wetting conditions.

III. A MODIFIED FLUID-WALL INTERACTION SCHEME

Although the fluid-wall interaction scheme of Li performs well for SC fluids, it is not straightforward to extend to PMM-CFs. For PMMCFs, the pseudopotential ψ depends on not only the fluid density ρ, but also the molar fraction c_i. However, due to the complex dependency of p_{EOS} on the molar fraction c_i, it is difficult to generate a guideline to tune ρ_w and $c_{w,i}$ at the same time to achieve a desired wetting condition.

In both the scheme of Benzi *et al.* [17] and the scheme of Li *et al.* [16], although the value of the virtual density ρ_w is adjusted, the ultimate goal is to define proper pseudopotential at the solid locations, i.e., ψ_w to control the wetting conditions. Following the idea of Li *et al.* to define the fluid-wall interaction using the local information [16], we propose a fluid-wall interaction scheme that reads

$$\mathbf{F}_w(\mathbf{x}) = -G\psi(\mathbf{x}) \sum_\alpha w_\alpha \psi_w(\mathbf{x} + \mathbf{e}_\alpha \delta_t) s(\mathbf{x} + \mathbf{e}_\alpha \delta_t) \mathbf{e}_\alpha, \quad (11)$$

where

$$\psi_w(\mathbf{x}) = \varphi \psi_{\text{ave}}(\mathbf{x}),$$

$$\psi_{\text{ave}}(\mathbf{x}) = \frac{\sum_\alpha w_\alpha s'(\mathbf{x} + \mathbf{e}_\alpha \delta_t)\psi(\mathbf{x} + \mathbf{e}_\alpha \delta_t)}{\sum_\alpha w_\alpha s'(\mathbf{x} + \mathbf{e}_\alpha \delta_t)}, \quad (12)$$

where φ is a parameter controlling the resulting contact angle in the simulations. With $\varphi > 1$, a contact angle $\theta < 90°$ is expected, and with $\varphi < 1$, $\theta > 90°$ is expected. The above equation is similar to the scheme of Li *et al.*, but differences exist in three key aspects. Instead of computing ψ_w through a properly defined virtual density (in the work of Li *et al.*), (in the proposed scheme) ψ_w is directly constructed. Second, a uniform scheme is used here for the whole range of contact angles from $0°$ to $180°$, in contrast with the scheme of Li *et al.* that uses two separate schemes for contact angles $\theta > 90°$ and $\theta < 90°$. Last, no limiter has been added to confine ψ_w. This is mainly to consider that the liquid and vapor densities would deviate from their saturated values with the existence of curved interfaces and associated capillary pressure. Alrthough these deviations are usually small, ψ_w is unconfined to reduce the artificial influence.

As ψ_w is defined directly by the modified scheme, this scheme is extendable to MC PP LB model for PMMCFs since there is no need to determine ρ_w and $c_{i,w}$ separately to obtain proper p_{EOS}. With the proposed fluid-wall interaction scheme, the resulting contact angle θ is found to linearly depend on the value of φ as

$$\cos\theta = -\frac{1}{2}(\varphi - 1)CGc_s^4 \frac{\delta t^3}{\delta x} \frac{(\psi_{v,\text{sat}}^2 - \psi_{l,\text{sat}}^2)}{\gamma_{lg}}, \quad (13)$$

where C is an empirical constant, $\psi_{l,\text{sat}}$ and $\psi_{g,\text{sat}}$ are the pseudopotential corresponding to the saturated liquid density and saturated vapor density, respectively. γ_{lg} is the liquid-vapor surface tension results from the PP LB model, which can be either computed analytically [1,24] or from the Young-Laplace equation in a simple case of a suspending droplet in a

gaseous environment. Alternatively, substituting the definition of ψ in Eq. (4) into the correlation proposed above, Eq. (13) can be rewritten in terms of the saturated vapor density $\rho_{v,\text{sat}}$ and the saturated liquid density as

$$\cos\theta = (\varphi - 1)Cc_s^4 \frac{\delta t^2}{\delta x} \frac{(\rho_{l,\text{sat}} - \rho_{v,\text{sat}})}{\gamma_{lg}}, \quad (14)$$

since the saturated vapor and liquid are corresponding to the same pressure.

The formulation of Eq. (13) can be explained as follows. According to Young's equation, the contact angle is determined by three surface tensions, i.e., the vapor-solid (vs) surface tension γ_{gs}, the liquid-solid (ls) surface tension γ_{ls}, and the liquid-vapor surface tension γ_{lg}, as

$$\cos\theta = \frac{\gamma_{gs} - \gamma_{ls}}{\gamma_{lg}}. \quad (15)$$

For PP LB models, the surface tension can be quantified as [30,31]

$$\gamma = \int_{-\infty}^{+\infty} (P_{xx} - P_{yy})dx = -\frac{1}{2}Gc_s^4\delta t^3 \int_{-\infty}^{+\infty} \left|\frac{d\psi}{dx}\right|^2 dx, \quad (16)$$

where P_{xx} and P_{yy} are the normal and transverse components of the pressure tensor, and the integral is from one bulk phase to another across an interface. Although it is difficult to use the above definition to compute the three surface tensions, we might use it to approximate them for the purposes of Eq. (13). As the fluid-wall interactions in the liquid and vapor phases are computed using the same scheme with the local information, it is reasonable to argue that the gradient of ψ has similar distribution and the two interfaces have close thickness. As a result, we will have

$$\int_{gs} \left|\frac{d\psi}{dx}\right|^2 dx \propto \frac{\psi_{v,\text{sat}}^2}{\delta x}, \quad \int_{ls} \left|\frac{d\psi}{dx}\right|^2 dx \propto \frac{\psi_{l,\text{sat}}^2}{\delta x}. \quad (17)$$

Using Eqs. (16) and (17) in Young's equation, we will have

$$\cos\theta \propto -\frac{1}{2}Gc_s^4 \frac{\delta t^3}{\delta x} \frac{\psi_{v,\text{sat}}^2 - \psi_{l,\text{sat}}^2}{\gamma_{lg}}. \quad (18)$$

In the proposed scheme, the parameter φ is deployed to control the resulting contact angle, which results in $\cos\theta > 0$ when $\varphi > 1$, i.e., $\theta < 90°$, and $\cos\theta < 0$ when $\varphi < 1$. Thus, the first guess of the dependency of $\cos\theta$ on φ can be performed as $\cos\theta \propto (\varphi - 1)$, which leads to

$$\cos\theta \propto -\frac{1}{2}(\varphi - 1)Gc_s^4 \frac{\delta t^3}{\delta x} \frac{\psi_{v,\text{sat}}^2 - \psi_{l,\text{sat}}^2}{\gamma_{lg}}. \quad (19)$$

By introducing a factor C for the above dependency and by replacing $\psi_{v,\text{sat}}$ and $\psi_{l,\text{sat}}$ in the above equation with the saturated densities $\rho_{v,\text{sat}}$ and $\rho_{l,\text{sat}}$, we finally reach the empirical correlation in Eq. (14). This empirical correlation was later found to predict the resulting contact angle well under various thermodynamic conditions with different PP LB models. The only two places in the correlation where input from the simulations were used are in the estimation of surface tension γ_{lg} and the constant C. Although the surface tension γ_{lg} can be determined via the EOS when the reduced temperature is selected, it could be more convenient to determine γ_{lg}

via simulations of a static droplet suspending in the vapor environment. The value of C is indeed determined by fitting in the simulation results, but it is also shown that the same value of C applies to different reduced temperatures, different EOS (limited to pure component cases), different choices of scaling, and different pseudopotential models. Therefore, the recommended values of C can be directly used by readers without performing extra simulations. The other parameters: $\rho_{l,\text{sat}}$ and $\rho_{v,\text{sat}}$ are readily obtained from applying the the Maxwell equal area rule for the isochemical potential condition, and they are already available for initialization and thermodynamic consistency examination. G, c_s, δ_x, and δ_t are just constants. By fitting in the results obtained in the following section, we recommend $C = -0.465$ for pure substance cases and $C = -0.45$ for MC partially miscible fluid cases.

IV. NUMERICAL TESTS

In this section, we would test the modified fluid-wall interaction scheme for handling wetting conditions in both the SC PP models and the MC PP model for PMMCFs, and validate the empirical correlation for contact angle predictions against the actual contact angles from the simulations. The case of a static droplet sitting on a smooth flat solid surface is adopted. The same case was also selected by many previous studies to examine the performances of fluid-wall interaction schemes in achieving wetting conditions [16,32] The computational domain is $N_x \times N_y = 400 \times 300$. The x direction is periodic, and the y direction is bounded by two solid walls. The halfway bounce-back scheme is used to implement the no-slip boundary condition on the two walls. Initially, a liquid droplet of radius $R_0 = 50$ is placed on the bottom wall. This initial condition is realized via a density field,

$$\rho(x, y, t = 0) = \frac{\rho_{l,\text{sat}} + \rho_{v,\text{sat}}}{2} - \frac{\rho_{l,\text{sat}} - \rho_{v,\text{sat}}}{2}$$
$$\times \tanh\left\{\frac{2[\sqrt{(x - x_c)^2 + (y - y_c)^2} - r_0]}{W}\right\}, \tag{20}$$

where $(x_c, y_c) = (N_x/2, 5)$ is the center location of the droplet and $W = 5$ is initial interface thickness. The reduced Peng-Robinson (PR) EOS for pure substances [21,29],

$$p_{\text{EOS}}^{\text{PR}} = \frac{\rho R_S T}{(1 - b\rho)} - \frac{a\alpha(T)\rho^2}{1 + 2b\rho - b^2\rho^2},$$
$$\alpha(T) = [1 + (0.374\,64 + 1.542\,26\omega - 0.269\,92\omega^2)$$
$$\times (1 - \sqrt{T/T_c})]^2 \tag{21}$$

is selected as p_{EOS} to compute ψ through Eq. (4), where T is the temperature, R_S is the specific gas constant, $a = 0.457\,24R_S T_c^2/p_c$, $b = 0.0778R_S T_c/p_c$ are the attractive and covolume parameters defined by the critical temperature T_c, the critical pressure p_c, and the specific gas constant R_S. ω is Pitzer's acentric factor of the cubic EOS. In our simulations, we choose $a = 1/49$, $b = 2/21$, $R_S = 1$ in LB units unless otherwise specified. The acentric factor of water $\omega = 0.344$ is selected.

Simulations are conducted with the MRT version of Li *et al.* of the forcing scheme [26] to restore thermodynamic consistency. This method is chosen because of its popularity. A free parameter σ in this scheme is adjusted to ensure the core region of the droplet has the same chemical potential as the vapor environment further away from the droplet. For the chosen reduced Peng-Robinson EOS, the chemical potential is calculated as

$$\mu^{\text{PR}}(\rho) = R_S T\left[\ln\left(\frac{\rho}{1 - b\rho}\right) + \frac{1}{1 - b\rho}\right]$$
$$- \frac{a\alpha}{2\sqrt{2}b}\ln\left[\frac{1 + (\sqrt{2} + 1)b\rho}{1 - (\sqrt{2} - 1)b\rho}\right] - \frac{a\alpha\rho}{1 + 2b\rho - b^2\rho^2}. \tag{22}$$

The kinematic viscosity is set to be 0.15 identically for both the vapor and the liquid phases. Except that τ_v is constrained by the kinematic viscosity ν as $\tau_v = \nu/(c_s^2\delta_t) + 0.5$, other relaxation times in the MRT collision operator are free to choose as long as numerical stability is ensured. Here we choose $\tau_\rho = \tau_j = 1.0$, $\tau_e = \tau_\varepsilon = 1.25$, and $\tau_q = 2/3$. We have performed extensive tests with other values of τ_e and τ_q, and with the single-relaxation time setting under different choices of kinematic viscosity, the results of the contact angles are only slightly affected. For the sake of conciseness, those results are not represented here.

The liquid-vapor surface tension γ_{lg} is needed to use the empirical correlation Eq. (13). In the present paper, γ_{lg} is numerically obtained from the case of a suspending droplet in vapor environment. This supporting case is conducted in a fully periodic domain of $N_x \times N_y = 300 \times 300$, with a liquid droplet fixed at the center of the domain. The other thermodynamics related parameters are chosen identical to the corresponding droplet-wall interaction case. A surface tension can be measured from the Young-Laplace law as $\gamma_{lg} = r\Delta p$ when the steady state is reached, where r is terminal droplet radius and Δp is the capillary pressure. To improve the accuracy, γ_{lg} used in Eq. (13) is averaged from four simulations with the initial droplet radii $r_0 = 30$, 40, 50, and 60.

First, we verify the ability of the proposed fluid-wall interaction scheme to achieve different wettability conditions. At $T = 0.8T_c$, the steady state density contours of three wetting conditions: $\theta \approx 60°$, $90°$, and $120°$ are shown in Figs. 1–3, respectively, for the proposed scheme and three aforementioned schemes proposed by Sukop and Thorne [13], Benzi *et al.* [17], and Li *et al.* [16]. The parameters, i.e., G_w in Sukop and Thorne's scheme, ρ_w in the scheme of Benzi *et al.*, ϕ and $\Delta\rho$ in the scheme of Li *et al.* are obtained via trial and error processes until the desired contact angles are achieved, whereas in the present scheme, the parameter φ is directly obtained from Eq. (14). For readers to reproduce those results, values of these parameters have been given in the caption of each figure. All four schemes are able to achieve those desired wetting conditions, but the two schemes using global constants to define fluid-wall interaction force result in nonphysical mass transfer layers between the droplet and solid surface, especially for cases with large contact angles, i.e., $\theta = 90°$ and $120°$. The two schemes using the local infor-
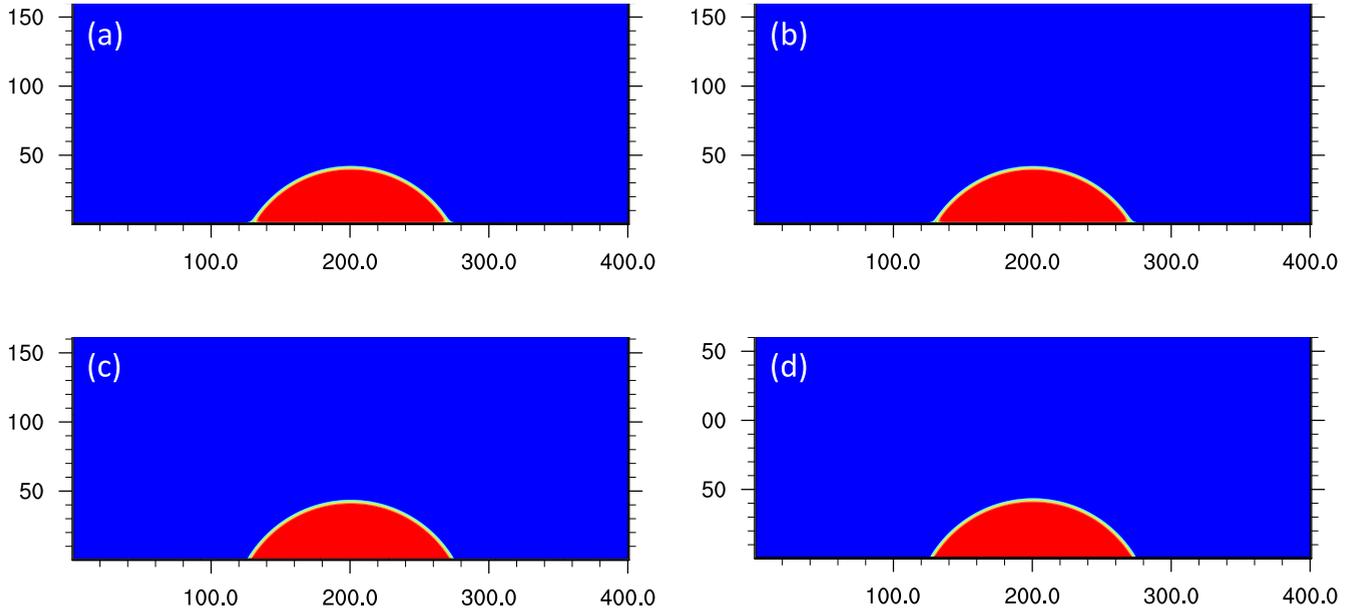
FIG. 1. Static contact angle $\theta \approx 60°$ by four tested fluid-wall interaction schemes: (a) Sukop and Thorne's scheme, (b) the scheme of Benzi *et al.*, (c) the scheme of Li *et al.*, and (d) the proposed scheme. The parameters are $G_w = -2.71$, $\rho_w = \rho_{v,\text{sat}} + 0.48(\rho_{l,\text{sat}} - \rho_{v,\text{sat}})\phi = 1.21$, $\Delta\rho = 0$, and $\varphi = 1.1$.

mation to define the fluid-wall interaction forces, on the other hand, are free of this issue.

It is also noteworthy that the two schemes using local information to define ψ_w generally result in better numerical stability than their counterparts using global constants. This is mainly due to two reasons. First, schemes using local information avoid having large gaps between ψ_w at wall locations and their neighboring fluid locations as pointed out by Li

et al. [16]. Second, large spurious currents, i.e., nonphysical velocities around the static interface, which are often regarded as one of the main causes for the numerical instability for PP LB models, are suppressed by the two schemes utilizing local information. From Figs. 4–6, the vector plots of the steady state velocity fields of the four fluid-wall interaction schemes are compared for the case of $\theta \approx 60°$, $90°$, and $120°$, respectively. The two schemes defining ψ_w with the local
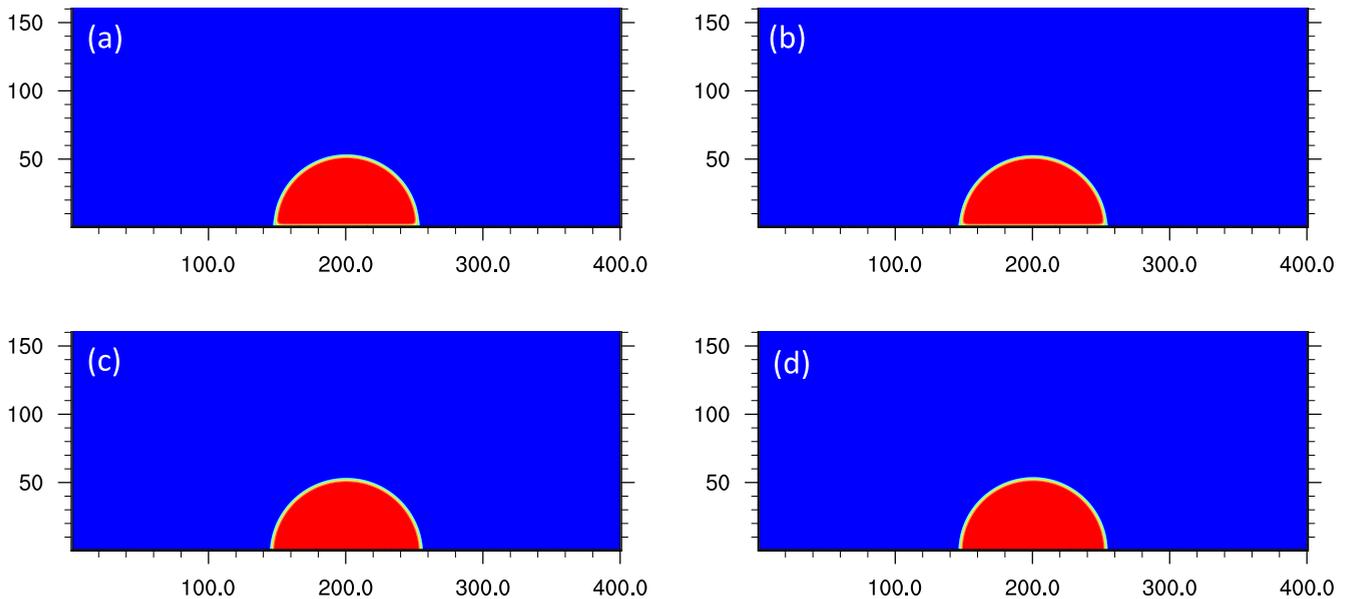
FIG. 2. Static contact angle $\theta \approx 90°$ by four tested fluid-wall interaction schemes: (a) Sukop and Thorne's scheme, (b) the scheme of Benzi *et al.*, (c) the scheme of Li *et al.*, and (d) the proposed scheme. The parameters are $G_w = -2.14$, $\rho_w = \rho_{v,\text{sat}} + 0.305(\rho_{l,\text{sat}} - \rho_{v,\text{sat}})$, $\phi = 1.0$, $\Delta\rho = 0$, and $\varphi = 1.0$.
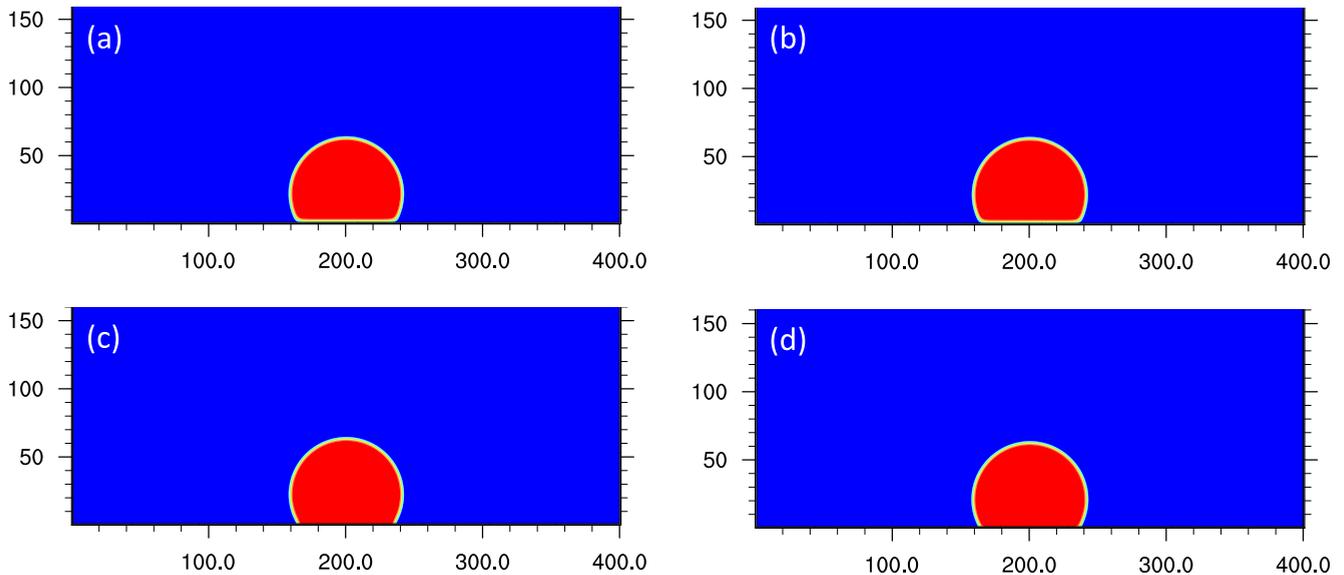
FIG. 3. Static contact angle $\theta \approx 120°$ by four tested fluid-wall interaction schemes: (a) Sukop and Thorne's scheme, (b) the scheme of Benzi *et al.*, (c) the scheme of Li *et al.*, and (d) the proposed scheme. The parameters are $G_w = -1.58$, $\rho_w = \rho_{v,\text{sat}} + 0.155(\rho_{l,\text{sat}} - \rho_{v,\text{sat}})$, $\phi = 1.0$ $\Delta\rho = 0.385$, and $\varphi = 0.9$.

information have much smaller spurious currents. In the case of $\theta = 120°$, the proposed scheme has even slightly less spurious currents compared to the scheme of Li *et al.*.

From now on, we focus on validating the empirical correlation Eq. (13) in predicting the contact angle against the actual contact angles obtained from the simulations. The generality of this correlation will be examined with different thermodynamic conditions and choices of PP LB models. As a start, a convergence study is conducted to ensure that the grid resolution, i.e., 400×300 is sufficient to provide reliable benchmark results of contact angles for comparisons. As shown in Fig. 7, the contact angles generated by different grid resolutions almost collapse with each other, which justifies the reliability of the numerical contact angles to serve as benchmark results.
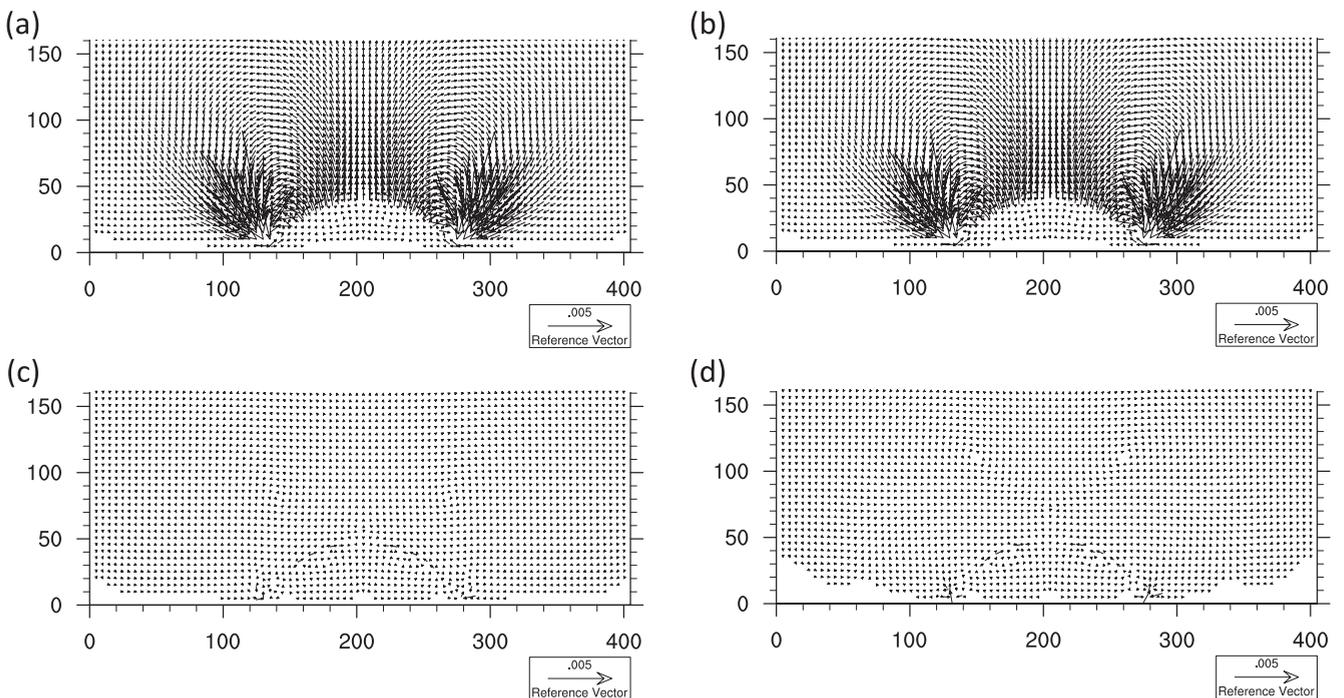
FIG. 4. Spurious currents around a static droplet of contact angle $\theta = 60°$ on a flat surface by four tested fluid-wall interaction schemes: (a) Sukop and Thorne's scheme, (b) the scheme of Benzi *et al.*, (c) the scheme of Li *et al.*, and (d) the proposed scheme.
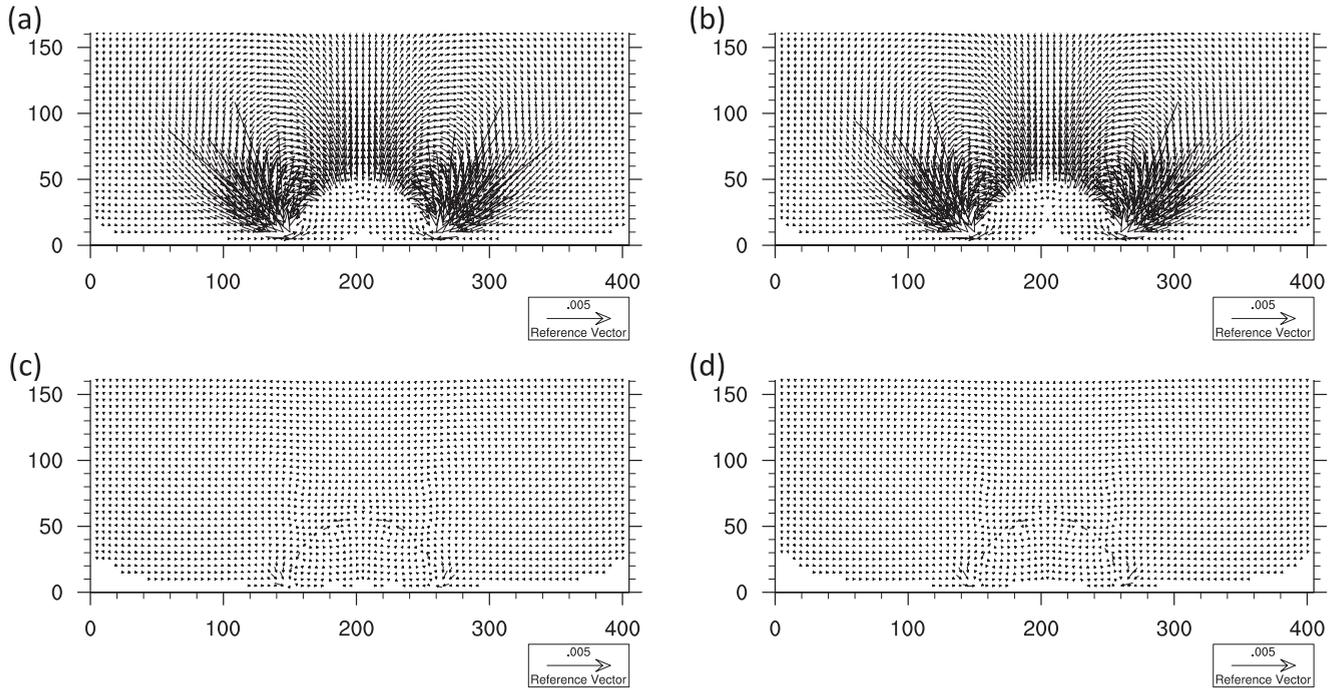
FIG. 5. Spurious currents around a static droplet of contact angle $\theta = 90°$ on a flat surface by four tested fluid-wall interaction schemes: (a) Sukop and Thorne's scheme, (b) the scheme of Benzi *et al.*, (c) the scheme of Li *et al.*, and (d) the proposed scheme.

For reduced PR EOS described in Eq. (21), the contact angles predicted from Eq. (13) are compared with the corresponding contact angles obtained from PP LB simulations in Fig. 8 under different temperatures. The liquid-to-vapor density ratios in these tests range from 10 at $T_r = 0.9$ to 870 at $T_r = 0.6$. It can be seen that the empirical correlation Eq. (13) results in good predictions of the contact angles in most examined cases with only a few exceptions with $\varphi - 1 \geqslant 0.25$ under $T_r = 0.6$ and 0.7 where the contact angles are overpredicted. The largest relative deviation is about 14%, which is still reasonably accurate.
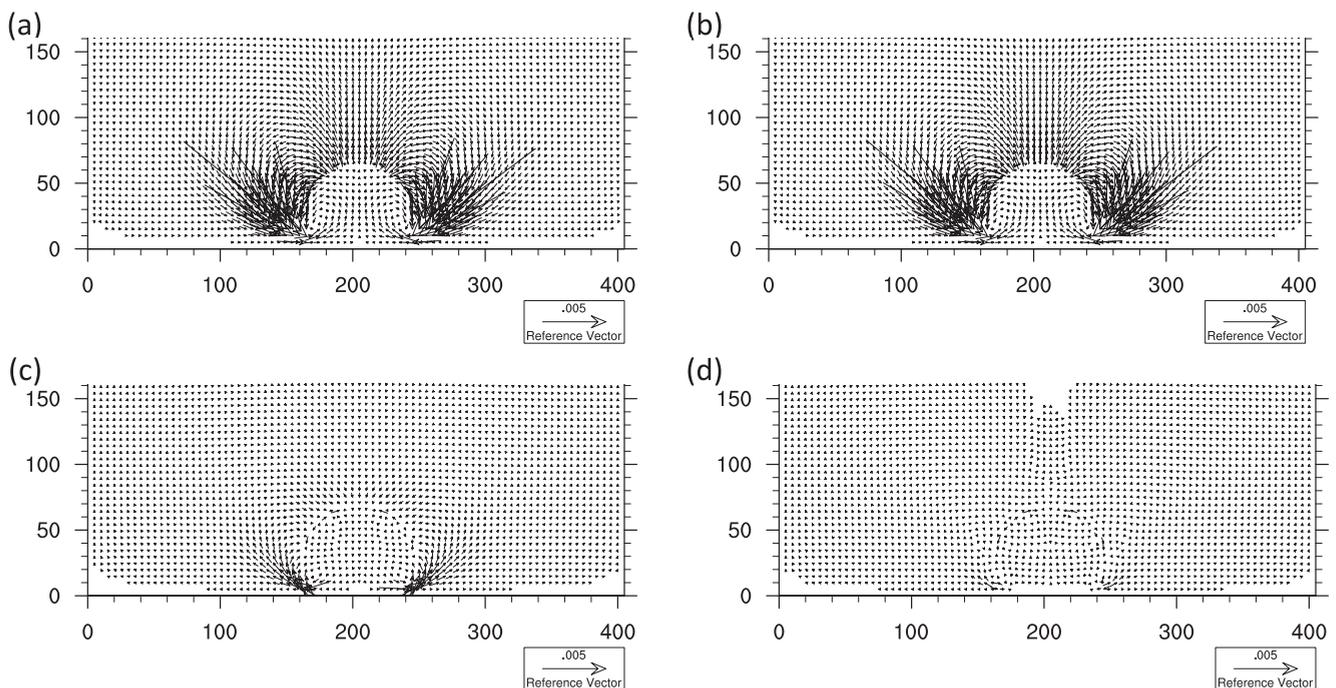
FIG. 6. Spurious currents around a static droplet of contact angle $\theta = 120°$ on a flat surface by four tested fluid-wall interaction schemes: (a) Sukop and Thorne's scheme, (b) the scheme of Benzi *et al.*, (c) the scheme of Li *et al.*, and (d) the proposed scheme.
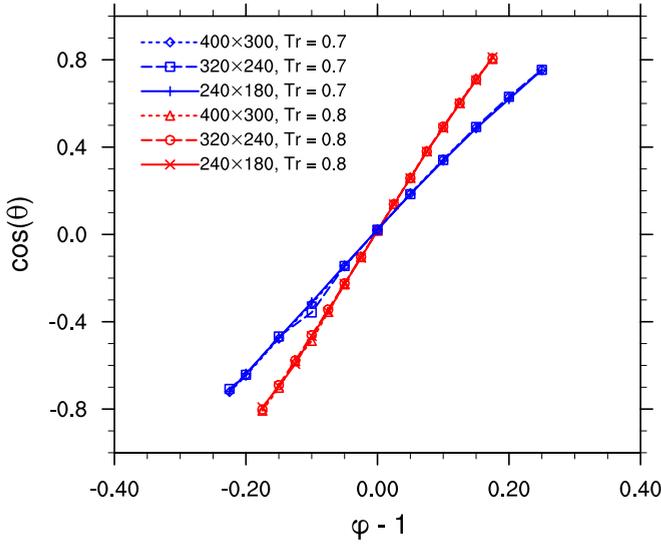
FIG. 7. The resulting contact angles with based on different grid meshes. The initial droplet radii are 30,–50 for the grid resolutions of 240×180, 320×240, and 400×300, respectively.

It should be pointed out that the proposed fluid-wall interaction scheme and the correlation of Eq. (13) have been validated for contact angles between $30°$ and $150°$. This range covers the contact angles of most realistic liquids on flat smooth surfaces. The proposed fluid-wall interaction scheme does not have difficulties to tackle very small contact angles ($\theta \to 0$) given a sufficiently large computational domain to re-
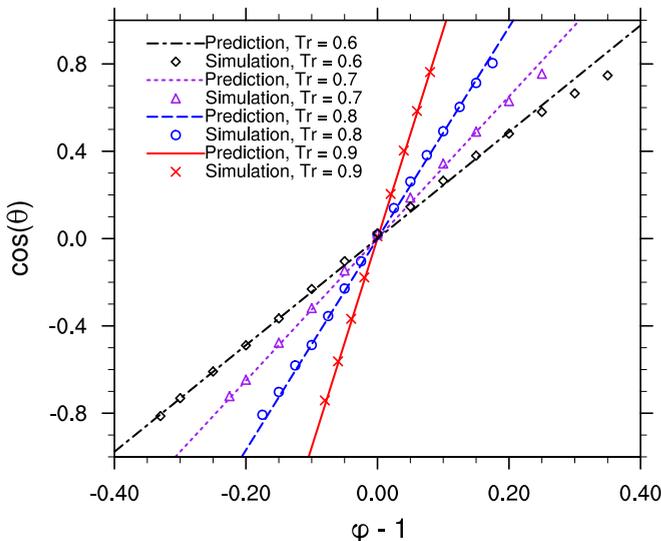
FIG. 8. The comparison between the actual contact angles from PP LB simulations and their expectations for the reduced PR EOS under different temperatures. Parameters (in LB units) used in the correlation: at $T_r = 0.9$, $\rho_{l,\text{sat}} = 5.908$, $\rho_{v,\text{sat}} = 0.5801$, $\gamma_{lg} = 0.028\,80$; at $T_r = 0.8$, $\rho_{l,\text{sat}} = 7.204$, $\rho_{v,\text{sat}} = 0.1971$, $\gamma_{lg} = 0.074\,74$; at $T_r=0.7$, $\rho_{l,\text{sat}}=8.080$, $\rho_{v,\text{sat}} = 0.055\,63$, $\gamma_{lg} = 0.1274$; at $T_r = 0.6$, $\rho_{l,\text{sat}} = 8.725$, $\rho_{v,\text{sat}} = 0.010\,23$, $\gamma_{lg} = 0.1844$.
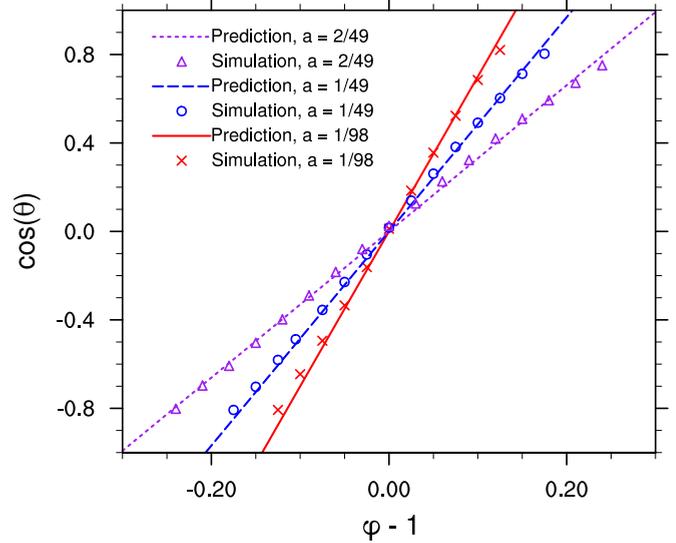
FIG. 9. The comparison between the actual contact angles from PP LB simulations and their expectations for different values of a in LB units. Parameters (in LB units) used in the correlation are $\rho_{l,\text{sat}} = 7.204$, $\rho_{v,\text{sat}} = 0.1971$, $\gamma_{lg} = 0.051\,69$, $0.074\,74$, and 0.1095 when $a = 1/98$, $1/49$, and $2/49$, respectively.

duce boundary confinement, but achieving very large contact angles ($\theta \to 180$) is found to be only possible with relatively small liquid-to-vapor density ratios. With relatively large density ratios, the droplet would detach from the wall rather than staying when very large contact angles are pursued. The same issue was also found in our own implementation of the fluid-wall interaction scheme of Li *et al.*, but was less profound with the other two schemes using global constants to define the fluid-wall interaction forces. This indicates a potential advantage of the latter two schemes in terms of wider range of achievable contact angles. However, as the proposed scheme and the scheme of Li *et al.* already covers the contact angles likely to be encountered in reality, their practical use is not affected.

Next, we show that the validity of Eq. (13) holds under various scalings between the physical parameters and their counterparts in LB units. Specifically, it has been well known that when using PP LB models, the attraction parameter a of the adopted EOS is subjected to adjustment in LB units to change the resulting surface tension and numerical stability. In Fig. 9, we compare the predicted and actual contact angles with three values of a, $a = 1/98$, $a = 1/49$, and $a = 2/49$ in PR EOS at $T_r = 0.8$. As clearly shown in the figure, good predictions of the contact angle are always obtained regardless of the choice of a, which further demonstrates the generality of the proposed correlation.

Equation (13) is also validated with different choices of cubic EOS. For other cubic EOS, e.g., the van der Waals (vdW) EOS,

$$p_{\text{EOS}}^{\text{vdW}} = \frac{\rho R_S T}{1 - b\rho} - a\rho^2, \quad a = \frac{27 R_S^2 T_c^2}{64 p_c}, \quad b = \frac{R_S T_c}{8 p_c}, \quad (23)$$
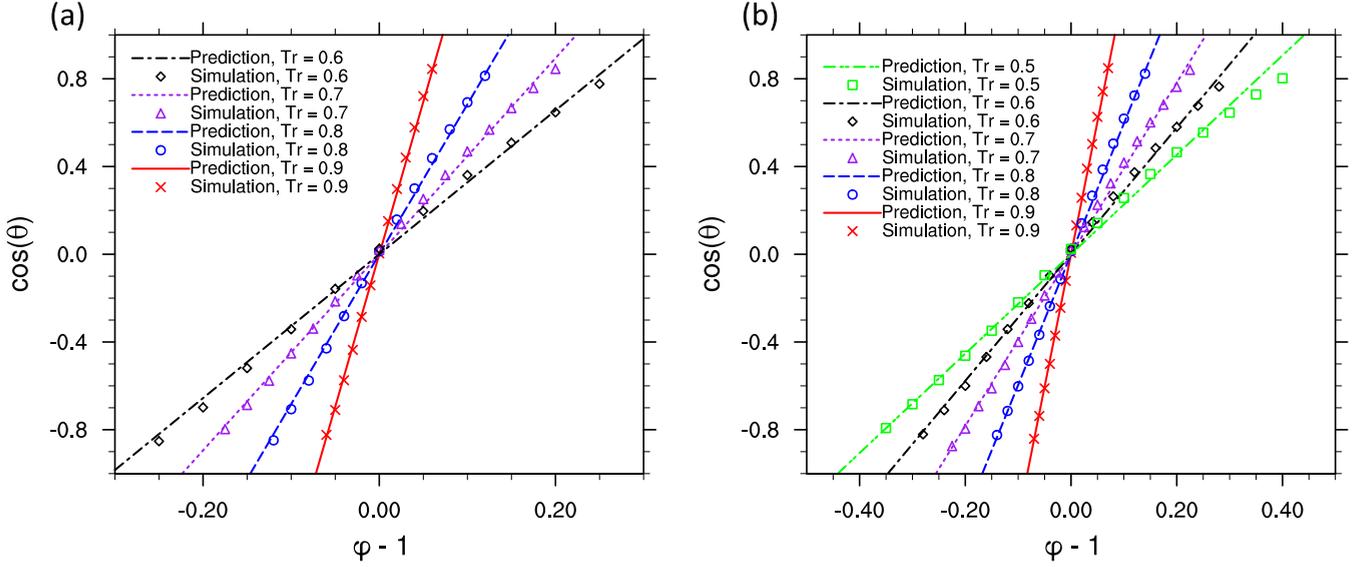
FIG. 10. The comparison between the actual contact angles from PP LB simulations and their expectations for different choices of cubic EOS: (a) vdW EOS, parameters (in LB units) used in the correlation: at $T_r = 0.9$, $\rho_{l,sat} = 5.800$, $\rho_{v,sat} = 1.490$, $\gamma_{lg} = 0.016\,02$; at $T_r = 0.8$, $\rho_{l,sat} = 6.764$, $\rho_{v,sat} = 0.8388$, $\gamma_{lg} = 0.044\,81$; at $T_r = 0.7$, $\rho_{l,sat} = 7.492$, $\rho_{v,sat} = 0.4481$, $\gamma_{lg} = 0.081\,39$; at $T_r = 0.6$, $\rho_{l,sat} = 8.090$, $\rho_{v,sat} = 0.2092$, $\gamma_{lg} = 0.1242$ in the LB units. (b) CS EOS, parameters used in the correlation: at $T_r = 0.9$, $\rho_{l,sat} = 0.2481$, $\rho_{v,sat} = 0.04543$, $\gamma_{lg} = 8.616 \times 10^{-4}$; at $T_r = 0.8$, $\rho_{l,sat} = 0.3072$, $\rho_{v,sat} = 0.021\,73$, $\gamma_{lg} = 2.463 \times 10^{-3}$; at $T_r = 0.7$, $\rho_{l,sat} = 0.3581$, $\rho_{v,sat} = 9.297 \times 10^{-3}$, $\gamma_{lg} = 4.585 \times 10^{-3}$; at $T_r = 0.6$, $\rho_{l,sat} = 0.4062$, $\rho_{v,sat} = 3.082 \times 10^{-3}$, $\gamma_{lg} = 7.192 \times 10^{-3}$; at $T_r = 0.5$, $\rho_{l,sat} = 0.4541$, $\rho_{v,sat} = 6.268 \times 10^{-4}$, $\gamma_{lg} = 0.010\,31$.

and the Carnahan-Starling (CS) EOS [33],

$$p_{EOS}^{CS}(\rho) = \rho R_S T \frac{1 + b\rho/4 + (b\rho/4)^2 - (b\rho/4)^3}{(1 - b\rho/4)^3} - a\rho^2,$$

$$a = 0.4963 \frac{R_S^2 T_c^2}{p_c}, \quad b = 0.18727 \frac{R_S T_c}{p_c}, \quad (24)$$

the contact angles predictions are compared with their actual values under different temperatures. Parameters (a, b, and R_S) in LB units are set to $a = 1/49$, $b = 2/21$, $R_S = 1$ for vdW EOS and $a = 1$, $b = 4$, $R_S = 1$ for CS EOS. As shown in Fig. 10, the correlation in Eq. (13) still performs exceptionally well regardless of EOS choice. The liquid-to-vapor density ratio from vdW EOS ranges from 4 to 40 in these tests, whereas the density ratio with CS EOS is between 5 and 720.

In the previous tests, the forcing scheme of Li *et al.* [26] is specifically used to ensure thermodynamic consistency is obtained. However, Eq. (13) still holds when other PP LB models are used. Besides the forcing scheme of Li *et al.*, the modified fluid-fluid interaction force proposed by Kupershtokh *et al.* [25] is also frequently utilized to restore thermodynamic consistency. Compare to the origin definition in Eq. (3), Kupershtokh *et al.* defined the fluid-fluid interaction force as [25]

$$\mathbf{F}(\mathbf{x}) = -\beta G \psi(\mathbf{x}) \sum_\alpha w_\alpha \psi(\mathbf{x} + \mathbf{e}_\alpha \delta_t) \mathbf{e}_\alpha$$

$$- \frac{1 - \beta}{2} G \sum_\alpha w_\alpha \psi^2(\mathbf{x} + \mathbf{e}_\alpha \delta_t) \mathbf{e}_\alpha, \quad (25)$$

where β is the tuning parameter, through adjusting which the thermodynamic consistency is restored. Correspondingly, the

fluid-wall interaction force should also be modified as

$$\mathbf{F}(\mathbf{x}) = -\beta G \psi(\mathbf{x}) \sum_\alpha w_\alpha \psi_w(\mathbf{x} + \mathbf{e}_\alpha \delta_t) s(\mathbf{x} + \mathbf{e}_\alpha \delta_t) \mathbf{e}_\alpha$$

$$- \frac{1 - \beta}{2} G \sum_\alpha w_\alpha \psi_w^2(\mathbf{x} + \mathbf{e}_\alpha \delta_t) s(\mathbf{x} + \mathbf{e}_\alpha \delta_t) \mathbf{e}_\alpha, \quad (26)$$

where ψ_w is still computed from Eq. (12).
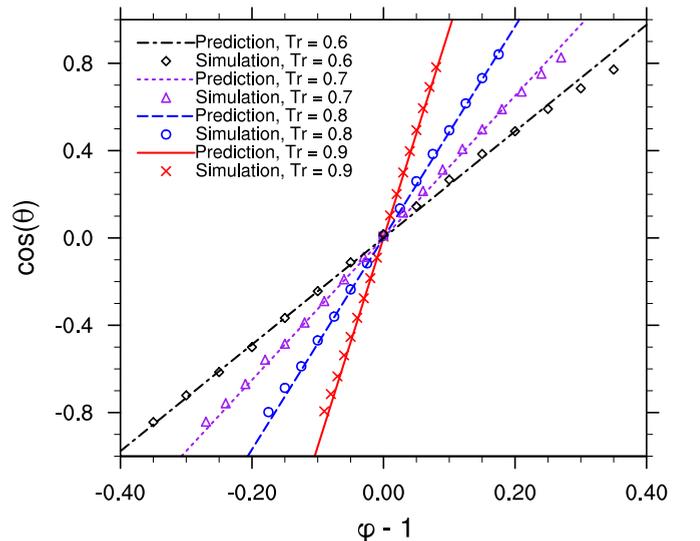
FIG. 11. The comparison between the actual contact angles from PP LB simulations with the modified definition of the interaction forces of Kupershtokh *et al.*. Parameters used in the correlation are as same as those in Fig. 8.

As shown in Fig. 11, the empirical correlation still holds when the model of Kupershtokh *et al.* is adopted. For the choice of the reduced PR EOS with $a = 1/49$, $b = 1/21$, $R = 1$, and $\omega = 0.344$, the predicted contact angles still match well with the actual values in the simulations. The value of β is tuned in each case to ensure the chemical potentials in the two bulk phases are always equal.

At last, the proposed fluid-wall interaction scheme and associated contact angle correlation are examined for the recently proposed MC PP LB model for PMMCFs. Unlike the thermodynamic equilibrium of pure substances where the liquid-vapor two-phase coexistence only establishes under a specific pressure at a given temperature, the two-phase coexistence of PMMCFs could happen over a range of pressures given a certain temperature. For validation purposes, here we examine the fluid-wall interaction schemes for four binary two-phase systems at the thermodynamic equilibrium, two systems of methane C_1 and propane C_3 mixtures, and the other two systems of propane C_3 and pentane nC_5 mixtures. The thermodynamic properties of these tested systems are given in Table I.

The MC PP LB simulations are again conducted with Li *et al.*'s forcing scheme [26] to ensure thermodynamic consistency. However, for MC PP LB models, the forcing term must be defined for each individual component. This means, once the total interaction force and the parts attributed to individual components have been defined, the forcing term $\mathbf{\Theta}_\eta$ is computed as

$$
\mathbf{\Theta}_\eta =
\begin{bmatrix}
0 \\
6\mathbf{F}_\eta \cdot \left(\mathbf{u} + \frac{\sigma \mathbf{F}}{(\tau_e - 0.5)c_s^2 \delta_t \psi^2} \right) \\
-6\mathbf{F}_\eta \cdot \left(\mathbf{u} + \frac{\sigma \mathbf{F}}{(\tau_\varepsilon - 0.5)c_s^2 \delta_t \psi^2} \right) \\
F_{\eta,x} \\
-F_{\eta,x} \\
F_{\eta,y} \\
-F_{\eta,y} \\
2(uF_{\eta,x} - vF_{\eta,y}) \\
uF_{\eta,y} + vF_{\eta,x}
\end{bmatrix},
\tag{27}
$$

where $\mathbf{F}_\eta = (F_{\eta,x}, F_{\eta,y})$ is the force attributed to component η, whereas $\mathbf{u}$ and $\mathbf{F}$ without the subscript are the velocity and interaction force subjected to the phase. The tuning parameter σ is again adjusted to ensure thermodynamic consistency is achieved. For MC partially miscible fluids, thermodynamic consistency is achieved by enforcing identical fugacities in the two bulk phases. For more details on the fugacity computation, readers may refer to Ref. [9].

The case of a staying droplet contacting with a flat solid wall is again adopted with the same domain size $N_x \times N_y = 400 \times 300$. The initial cell-volume density field for the *i*th component is defined as

$$
\bar{\rho}_i(x, y, t = 0) = \frac{\bar{\rho}_{i,l,\text{sat}} + \bar{\rho}_{i,v,\text{sat}}}{2} + \frac{\bar{\rho}_{i,l,\text{sat}} - \bar{\rho}_{i,v,\text{sat}}}{2}
$$
$$
\times \tanh \left[\frac{2(\sqrt{(x - x_c)^2 + (y - y_c)^2} - R_0)}{W} \right],
\tag{28}
$$

TABLE I. Thermodynamic properties of tested binary systems. Top table: the thermodynamic properties of individual components from left to right: component, critical pressure, critical temperature, Pitzer's acentric factor, and molar mass [27]. Bottom table: the thermodynamic properties of binary systems at thermodynamic equilibrium from left to right: temperature, pressure, molar fraction of the first component in the liquid phase ($x_2 = 1 - x_1$), molar fraction of the first component in the vapor phase ($y_2 = 1 - y_1$), the mass density of the liquid phase, and the mass density of the vapor phase.

	p_{ci} (psia)	T_{ci} ($^\circ R$)	ω_i	M_i
C_1	666.40	343.33	0.0104	16.043
C_3	616.00	666.06	0.1522	44.097
nC_5	488.60	845.80	0.2514	72.150

Components	T (R°)	p (psia)	x_1	y_1	$\rho_{l,\text{sat}}$ (lb/ft^3)	$\rho_{v,\text{sat}}$ (lb/ft^3)
$C_1 + C_3$	530	500	0.16914	0.66363	29.478	2.8507
$C_1 + C_3$	430	200	0.12906	0.87844	36.458	0.92650
$C_3 + nC_5$	580	40	0.40175	0.83732	35.719	0.88778
$C_3 + nC_5$	550	40	0.20193	0.72287	38.441	0.37389

where $\bar{\rho}_{i,l,\text{sat}}$, $\bar{\rho}_{i,v,\text{sat}}$ are computed based on the material balance as

$$
\bar{\rho}_{i,l,\text{sat}} = \rho_{l,\text{sat}} \frac{x_i M_i}{\sum_i x_i M_i}, \qquad \bar{\rho}_{i,v,\text{sat}} = \rho_{v,\text{sat}} \frac{y_i M_i}{\sum_i y_i M_i}.
\tag{29}
$$

The comparison between the predicted contact angles from Eq. (13) and their corresponding contact angles captured from simulations for the selected are shown in Fig. 12 for the selected PMMCF systems. The comparisons clearly
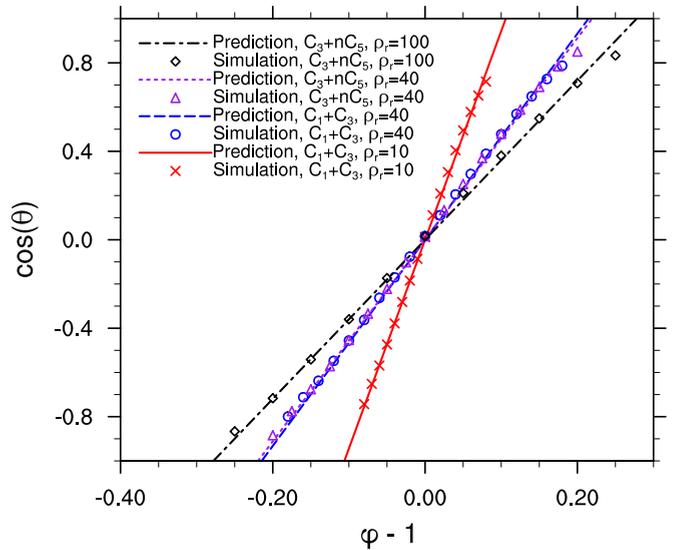
FIG. 12. The comparison between the actual contact angles from PP LB simulations with partially miscible MC hydrocarbon fluids. Parameters used in the correlation (in LB units), case 1: $\rho_{l,\text{sat}} = 8.297$, $\rho_{v,\text{sat}} = 0.8024$, $\gamma_{lg} = 0.039\,51$; case 2: $\rho_{l,\text{sat}} = 10.26$, $\rho_{v,\text{sat}} = 0.2608$, $\gamma_{lg} = 0.1098$; case 3: $\rho_{l,\text{sat}} = 7.677$, $\rho_{v,\text{sat}} = 0.1908$, $\gamma_{lg} = 0.081\,86$; case 4: $\rho_{l,\text{sat}} = 8.262$, $\rho_{v,\text{sat}} = 0.080\,36$, $\gamma_{lg} = 0.1133$.

demonstrate that not only the proposed scheme can handle the wetting conditions for PMMCFs, but also the resulting contact angles are still very well predicted by the proposed correlation.

V. CONCLUSIONS

In this paper, we proposed a modified fluid-wall interaction scheme to handle wetting conditions for PP LB models. This scheme is not only able to capture a wide rage of contact angles with SC PP LB models, but also works well with the recently developed MC PP LB model applied to PMMCFs, which further expands the application of PP LB models to important multiphase flow simulation scenarios. Compared to the other schemes restricted to SC PP LB models, the proposed scheme eliminated the nonphysical mass transfer layer between the staying droplet and the solid surface and

further suppressed spurious currents around the liquid-vapor interfaces.

Based on the proposed scheme, a contact angle correlation was developed to predict the resulting static contact angles. The validity of the proposed correlation had been examined for a wide variety of thermodynamic conditions, including different temperatures, different choices of pressure scaling, different cubic EOSs, and different PP LB models, including two widely selected SC PP LB models and the recently developed MC PP LB model for PMMCFs. The utility of using this correlation to eliminate painful trial and error in order to achieve any desired wetting conditions has been fully demonstrated.

[1] H. Huang, M. Sukop, and X. Lu, *Multiphase Lattice Boltzmann Methods: Theory and Application* (Wiley, Hoboken, NJ, 2015).

[2] X. Shan and H. Chen, Lattice boltzmann model for simulating flows with multiple phases and components, Phys. Rev. E **47**, 1815 (1993).

[3] X. Shan and H. Chen, Simulation of nonideal gases and liquid-gas phase transitions by the lattice boltzmann equation, Phys. Rev. E **49**, 2941 (1994).

[4] L. Chen, Q. Kang, Y. Mu, Y.-L. He, and W.-Q. Tao, A critical review of the pseudopotential multiphase lattice boltzmann model: Methods and applications, Int. J. Heat Mass Transf. **76**, 210 (2014).

[5] Q. Li, K. H. Luo, Q. Kang, Y. He, Q. Chen, and Q. Liu, Lattice boltzmann methods for multiphase flow and phase-change heat transfer, Prog. Energy Combust. Sci. **52**, 62 (2016).

[6] X. Shan and G. Doolen, Multicomponent lattice-boltzmann model with interparticle interaction, J. Stat. Phys. **81**, 379 (1995).

[7] N. S. Martys and H. Chen, Simulation of multicomponent fluids in complex three-dimensional geometries by the lattice boltzmann method, Phys. Rev. E **53**, 743 (1996).

[8] B. Gong, X. Liu, and G. Qin, A lattice boltzmann model for multi-component vapor-liquid two phase flow, Pet. Explor. Dev. **41**, 695 (2014).

[9] C. Peng, L. F. Ayala, and O. M. Ayala, A thermodynamically consistent pseudo-potential lattice boltzmann model for multicomponent, multiphase, partially miscible mixtures, J. Comput. Phys. **429**, 110018 (2021).

[10] K. S. Pedersen, P. L. Christensen, and J. A. Shaikh, *Phase Behavior of Petroleum Reservoir Fluids* (CRC, Boca Raton, FL, 2006).

[11] W. D. McCain, Jr., *Properties of Petroleum Fluids* (PennWell Corp., Tulsa, OK, 2017).

[12] P. Raiskinmäki, A. Shakib-Manesh, A. Jäsberg, A. Koponen, J. Merikoski, and J. Timonen, Lattice-boltzmann simulation of capillary rise dynamics, J. Stat. Phys. **107**, 143 (2002).

[13] M. C. Sukop and D. T. J. Thorne, *Lattice Boltzmann Modeling: An Introduction for Geoscientists and Engineers* (Springer, Berlin, 2006).

[14] H. Huang, Z. Li, S. Liu, and X.-Y. Lu, Shan-and-chen-type multiphase lattice boltzmann study of viscous coupling effects for two-phase flow in porous media, Int. J. Numer. Methods Fluids **61**, 341 (2009).

[15] Q. Li, K. H. Luo, Q. J. Kang, and Q. Chen, Contact angles in the pseudopotential lattice boltzmann modeling of wetting, Phys. Rev. E **90**, 053301 (2014).

[16] Q. Li, Y. Yu, and K. H. Luo, Implementation of contact angles in pseudopotential lattice boltzmann simulations with curved boundaries, Phys. Rev. E **100**, 053313 (2019).

[17] R. Benzi, L. Biferale, M. Sbragaglia, S. Succi, and F. Toschi, Mesoscopic modeling of a two-phase flow in the presence of boundaries: The contact angle, Phys. Rev. E **74**, 021509 (2006).

[18] X. He and L.-S. Luo, Theory of the lattice Boltzmann method: From the Boltzmann equation to the lattice Boltzmann equation, Phys. Rev. E **56**, 6811 (1997).

[19] P. Lallemand and L.-S. Luo, Theory of the lattice Boltzmann method: Dispersion, dissipation, isotropy, Galilean invariance, and stability, Phys. Rev. E **61**, 6546 (2000).

[20] Z. Guo, C. Zheng, and B. Shi, Discrete lattice effects on the forcing term in the lattice Boltzmann method, Phys. Rev. E **65**, 046308 (2002).

[21] P. Yuan and L. Schaefer, Equations of state in a lattice boltzmann model, Phys. Fluids **18**, 042101 (2006).

[22] C. E. Colosqui, G. Falcucci, S. Ubertini, and S. Succi, Mesoscopic simulation of non-ideal fluids with self-tuning of the equation of state, Soft Matter **8**, 3798 (2012).

[23] Q. Li, K. H. Luo, and X. J. Li, Forcing scheme in pseudopotential lattice Boltzmann model for multiphase flows, Phys. Rev. E **86**, 016709 (2012).

[24] C. Peng, L. F. Ayala, Z. Wang, and O. M. Ayala, Attainment of rigorous thermodynamic consistency and surface tension in single-component pseudopotential lattice boltzmann models

via a customized equation of state, Phys. Rev. E **101**, 063309 (2020).

[25] A. Kupershtokh, D. Medvedev, and D. Karpov, On equations of state in a lattice boltzmann method, Comput. Math. Appl. **58**, 965 (2009).

[26] Q. Li, K. H. Luo, and X. J. Li, Lattice Boltzmann modeling of multiphase flows at large density ratio with an improved pseudopotential model, Phys. Rev. E **87**, 053301 (2013).

[27] A. Danesh, *PVT and Phase Behaviour of Petroleum Reservoir Fluids* (Elsevier, Amsterdam, 1998), Vol. 47.

[28] T. Ertekin and L. F. Ayala, *Reservoir Engineering Models: Analytical and Numerical Approaches* (McGraw-Hill, New York, 2018).

[29] D.-Y. Peng and D. B. Robinson, A new two-constant equation of state, Ind. Eng. Chem. Fundam. **15**, 59 (1976).

[30] X. He and G. D. Doolen, Thermodynamic foundations of kinetic theory and lattice boltzmann models for multiphase flows, J. Stat. Phys. **107**, 309 (2002).

[31] X. Shan, Pressure tensor calculation in a class of nonideal gas lattice boltzmann models, Phys. Rev. E **77**, 066702 (2008).

[32] H. Huang and X.-Y. Lu, Relative permeabilities and coupling effects in steady-state gas-liquid flow in porous media: A lattice boltzmann study, Phys. Fluids **21**, 092104 (2009).

[33] N. F. Carnahan and K. E. Starling, Equation of state for nonattracting rigid spheres, J. Chem. Phys. **51**, 635 (1969).